Granular Matter (2010) 12:287–301
DOI 10.1007/s10035-010-0180-0

Shear banding and strain softening in plane strain extension: physical modelling

L. Röchter · D. König · T. Schanz · T. Triantafyllidis

Received: 3 May 2009 / Published online: 3 April 2010

Abstract Localization of deformation in systems of shear bands or normal faults, respectively, as a consequence of extensional loading can be observed on a wide range of spatial scales in soil and rock formations. A series of plane strain model experiments was achieved in natural (1 g) and increased (ng) gravity field (geotechnical centrifuge) with dry and moist sand as well as with dry and moist sand-clay mixtures. In these experiments, the geometry of the shear bands (inclination, width, spacing, sharpness) was detected by means of the digital image correlation (DIC) technique. Comparison with existing analytical approaches for the determination of the spacing of shear bands is presented briefly. The stress-strain behaviour of the materials was determined in a new biaxial test device, which allows for the performance of biaxial compression and extension tests. The evaluation focuses on the strain softening gradient, which is seen as a key parameter in the explanation of shear band spacing.

Keywords Shear band patterns · Cohesive-frictional material · Physical modelling · Plane strain extension · Strain softening

L. Röchter (✉) · D. König · T. Schanz
Chair for Foundation Engineering, Soil and Rock Mechanics, Ruhr-Universität Bochum, Universitätsstr. 150, 44801 Bochum, Germany
e-mail: lars.roechter@rub.de

T. Triantafyllidis
Institute of Soil Mechanics and Rock Mechanics, Universität Karlsruhe (TH), Engler-Bunte-Ring 14, 76131 Karlsruhe, Germany

1 Introduction

1.1 Shear band systems in situ, in physical and numerical modelling

Localization of deformation in a system of shear bands or normal faults, respectively, as a consequence of extensional loading was reported on different spatial scales. On macro scale (10^2–10^4 m), systems of parallel normal faults were documented in many extensional regions of the upper earth crust [5,26,32,37,53,63,64,71]. Only McIntosh et al. [32] and Morellato et al. [37] presented quantitative data concerning the spacing of normal faults in situ. Numerous researchers addressed patterns of localization of deformation in physical experiments on meso scale (10^{-2}–10^{-1} m). Different extensional mechanisms were applied in the field of experimental and numerical studies, such as stretching of a horizontal basement [5,16,18,20,30,31,42,57], stretching of an inclined basement [6,58], imposing a discontinuity in the strain field [9,12,16,38] or upward bending of the basement [6,7]. But also in this field, only limited attention was paid to the quantitative determination of shear band spacing. In fact, only Leśniewska and Mróz [23,24] and Wolf et al. [66–69] investigated this interesting topic. Wolf et al. investigated systematically the influence of specimen's height, granulometric properties, stress level and density, using dry sand as model material. In this study, the process of localization of deformation was investigated in a broad range of material compositions, using dry and moist sand as well as dry and moist sand-clay mixtures as model material. The hitherto achieved large data base of about 60 model experiments allows for the analysis of shear band spacing depending on certain characteristics of the model material.

1.2 Analytical explanation of shear band spacing in physical modelling

The following three analytical approaches have been developed to explain the spacing in a system of parallel shear bands. Leśniewska [23,24] developed an analytical approach for the calculation of the spacing of shear bands behind a rotating retaining wall. A fundamental assumption is that localization in multiple shear bands is a progressive process. According to her results, strain softening inside the shear bands is crucial for the development of a shear band system. Leśniewska further concluded that the greater the softening modulus is, the larger the spacing will be. Strain softening is defined as the reduction of the mobilized friction angle from the peak value to the critical value with increasing displacement of a soil wedge along the shear band. In order to verify this approach, Leśniewska referred to experiments of Milligan [34]. The shear band spacing was successfully calculated for dense sand [24]. A smaller spacing in the experiments with loose sand, as predicted by the analytical model, could not be observed.

Mandl [26] presented an idea for the explanation of the spacing in sandbox extension experiments, in which an underlying layer is stretched. According to Mandl, the localization of deformation is accompanied by a decrease of shear stress from the limit stress state to a smaller stress state with ongoing shearing. The blocks between the initial localization zones are elastically unloaded by an increase of the horizontal stress $\sigma_h = \sigma_3$. Strain softening as a brittleness parameter was defined as $|-\mathrm{d}\varphi/\mathrm{d}\kappa|$ with $\kappa = \int \mathrm{d}\gamma_{pl}$. Mandl also assumed a progressive failure process with faults appearing consecutively between the initial faults, finally resulting in a minimum distance. He concluded that in materials with greater softening, i.e. more brittle behaviour, the elastic energy release is larger and therefore a wider region is elastically unloaded, which results in a larger spacing between the localization zones. On the other hand, the spacing is expected to be smaller in materials in which the elastic reloading as a consequence of further stretching of the underlying layer, is faster. This finally ends up in a competition between strain softening and elastic modulus.

Wolf [66] developed an analytical approach for the calculation of the spacing, based on the observation of a simultaneous onset of parallel shear bands. After the onset of localization, the deformation is concentrated inside the shear bands, whereas the blocks between the shear bands rotate in the direction of stretching. This approach starts from the mode of failure prescribed in a set of parallel shear bands. The width of the blocks, which maximizes the dissipated energy of the whole system, is calculated considering shearing, dilation and softening inside the shear band and elastic unloading outside the shear band. Without strain softening, defined as $k = -\mathrm{d}\varphi/\mathrm{d}|\gamma|$, no localization of multiple shear bands is possible. Wolf concluded that the spacing is smaller when the softening is more pronounced, which he confirmed in experiments with dense and loose sand.

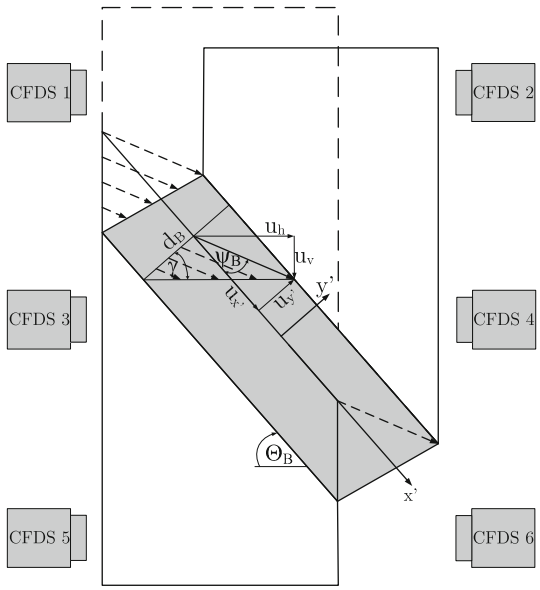

Fig. 1 Geometry and deformation inside shear band (exaggerated), modified after Drescher et al. [11]. Positions of contact free displacement sensors (CFDS) in a new biaxial device (Sect. 4.1)

1.3 Localization of deformation in a single shear band

The localization of deformation in a system of shear bands requires understanding concerning the failure process in a single shear band. The principal mechanism is explained referring to the sketch by Drescher et al. [11], modified in Fig. 1. Before the shear band develops, the specimen deforms homogeneously. After the onset of shear banding, the deformation localizes inside the shear band, whereas the material outside the shear band unloads elastically (Hayano [17]), often assumed as rigid (e.g. Drescher et al. [11]). The shear band deforms in simple shear mode, which corresponds to a weak discontinuity mode of the specimen, i.e. the displacement field shows a kink at the border between inside and outside the shear band. The inclination of the shear band θ with respect to the minor principal stress axis can be calculated according to Roscoe [50] with Eq. 1, to Coulomb [8] with Eq. 2 or to Arthur et al. [3] with Eq. 3. The solution according to Roscoe θ_R represents a lower bound, the solution according to Coulomb θ_C represents an upper bound, and the solution according to Arthur θ_A, which was also proposed by Vardoulakis [56] applying bifurcation analysis, is an intermediate solution between θ_R and θ_C.

$$\theta_R = 45^\circ + \psi_p/2 \tag{1}$$

$$\theta_C = 45^\circ + \varphi'_p/2 \tag{2}$$

$$\theta_A = 45^\circ + (\varphi'_p + \psi_p)/4 \tag{3}$$

Herein, φ'_p represents the maximum friction angle and ψ_p the dilatancy angle at the maximum friction angle.

$$\varphi'_p = \arcsin\left(\frac{\sigma'_1 - \sigma'_3}{\sigma'_1 + \sigma'_3}\right) \tag{4}$$

$$\psi_p = \arcsin\left(\frac{\dot{\varepsilon}_v}{\dot{\gamma}}\right) \tag{5}$$

Within this study, the major principal stress σ'_1 is the vertical stress in the model experiments, whereas it is the horizontal stress in the plane strain extension tests. The minor principal stress σ'_3 represents the horizontal stress in the direction of prescribed displacement in the model experiments, whereas it is the vertical stress in the plane strain extension tests. The shear band thickness d_B usually is given as a multiple of the mean grain size d_{50}, in the range of 7–22 d_{50} (e.g. [10,33,43,74]).

According to Wanatowski and Chu [59,60], shear banding and accompanied strain softening is a response of the soil under plane-strain boundary conditions, whereas in drained triaxial compression tests, shear banding is strongly affected by friction between specimen and end platens. This is a fundamental difference between axial symmetric and plane strain boundary conditions. Compared to triaxial and biaxial compression tests, triaxial extension tests are more difficult to perform (Wu and Kolymbas [70], Yamamuro and Lade [73], Yamamuro and Liu [72]). Biaxial or plane strain extension tests, including one pair of flexible walls, are rare. In fact, only very few plane strain extension tests were carried out by Masuda et al. [29]. Since systematic differences were found between triaxial and biaxial compression tests (Green [14], Lade and Duncan [22], Reades and Green [48], Marachi et al. [27], Peters et al. [45], Schanz and Vermeer [51], Alshibli et al. [2], Wanatowski and Chu [60]), similar differences have been suspected by the authors between triaxial and biaxial extension tests. Since the strain softening behaviour is supposed to influence the developing shear band systems strongly [23,26,69], element tests under the same boundary conditions as they are present in the model experiments, i.e. plane strain extension, were required. Therefore, we constructed a new device for the performance of plane strain compression and extension tests. The strain softening behaviour, which is accompanied by localization of deformation inside a shear band, does not represent a characteristic of a material element, since the homogeneity of strains is lost with the onset of shear banding. We are more interested in the strain softening inside the shear band. The influence of the specimen's height on the softening behaviour associated with strain localization inside a shear band was shown by Tatsuoka et al. [54]. Modelling the stress-strain relation of Toyoura Sand in plane strain compression tests, they concluded that a larger specimen's height is accompanied by a more pronounced softening, i.e. by a steeper stress-(averaged) strain curve in the post-peak regime. A unique relationship between shear stress level and shear displacement inside the shear band, normalized by d_{50}, was documented by Yoshida et al. [74], who performed biaxial compression tests with seven sands of identical specimen height. According to Tatsuoka et al. [54], the shear strain averaged for the specimen height is a function of the ratio d_{50}/h. Thus, the post-peak softening of the specimen is more pronounced the smaller the ratio of the shear band area, in terms of d_{50}, to the specimen area, in terms of h, is.

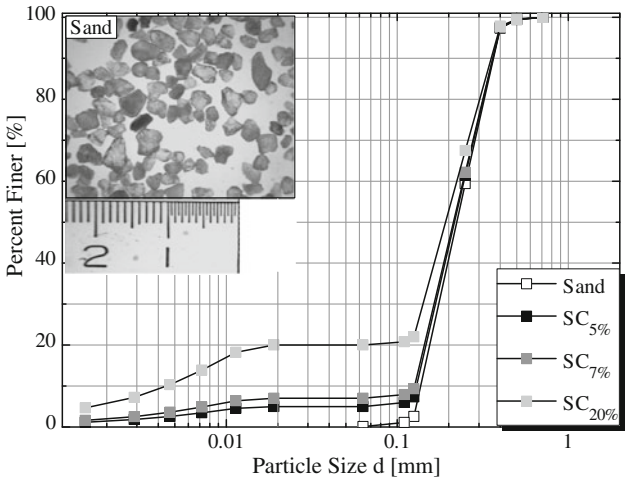

Fig. 2 Grain size distribution curve of Silversand and sand-clay- mixtures

2 Model material

2.1 Basic materials

A broad range of material compositions was investigated in the present study (Table 3), the basic components were Silversand, Kaolin clay and water.

2.1.1 Silversand

As basic material, so called Silversand was used (excavation location is the lake Silver in Germany). Silversand is a quartz sand (99 % SiO_2) with rounded grains within a range of 0.06–0.71 mm (Fig. 2). The basic properties are summarized in Table 1.

2.1.2 Kaolin clay

The laboratory analysis reveals that the Kaolin clay is dominated by the silt fraction according to the classification by Casagrande (Table 2).

Table 1 Basic properties of Silversand

d mm	d_{50} mm	C_U –	$\rho_{d,min}$ g/cm^3	$\rho_{d,max}$ g/cm^3	e_{max} –	e_{min} –	ρ_s g/cm^3
0.06–0.71	0.23	1.8	1.399	1.709	0.901	0.556	2.65

Table 2 Basic properties of Kaolin clay

w_P %	w_L %	I_P %	ρ_s g/cm^3	w_{Pr} %	ρ_{Pr} g/cm^3
28.2	46.6	18.4	2.70	25.5	1.55

Table 3 Material compositions tested within this study

Material composition	Material symbol	Sand (%)	Clay (%)	Water (%)	c (kPa)	ρ_d (g/cm^3)	D_r or R_c, resp. (−)
S	□	100.0	0.0	0.0	0.0	1.64–1.67	0.81–0.91
$SC_{5\%}$	■	95.0	5.0	0.0	0.2	1.66–1.72	1.01–1.05
$SC_{7\%}$	■	93.0	7.0	0.0	0.6	1.65–1.68	0.98–1.00
$SC_{20\%}$	■	80.0	20.0	0.0	2.3	1.62–1.68	0.85–0.88
$SW_{1\%}$	▣	99.0	0.0	1.0	0.8	1.46–1.48	0.93–0.95
$SW_{5\%}$	▣	95.0	0.0	5.0	1.8	1.51– 1.57	0.95–0.97
$SC_{4\%}W_{1.7\%}, md$	▤	94.3	4.0	1.7	2.0	1.51–1.52	0.91–0.95
$SC_{4\%}W_{1.7\%}, d$	▤	94.3	4.0	1.7	2.6	1.59–1.70	0.98–1.06

Square frames represent dense Silversand, colored symbols represent dry sand-clay mixtures, framed symbols represent sand-water mixtures, and framed symbols consisting of two colors represent sand-clay-water mixtures. In addition to the dry density ρ_d (range, which was achieved in cohesion and biaxial tests as well as in the model experiments), the relative density $D_r = (e_{max} - e)/(e_{max} - e_{min})$ is given for dense sand, whereas the relative compaction $R_c = \rho_d/\rho_{Proctor}$ is given for the material compositions. The indices md and d indicate medium dense and dense specimens. The indicated Kaolin clay fraction actually represents the finegrained fraction, which is composed by 30% clay and 70% silt size fraction. E.g. $SC_{20\%}$ indicates a finegrained fraction of 20%, resulting in a clay size fraction of 6% by weight

2.2 Cohesive-frictional material compositions

A small cohesive strength, in the sense that these specimens were able to stand vertically unsupported, was produced by adding small amounts of clay or water or both to the Silversand (similar mixtures were used by Mélix [36]). This additional strength is created by matric suction, particle interlocking, bonding of clay particles as well as bonding of clay with silt and sand particles (Mitchell and Soga [35]). These effects are summarized as (apparent) cohesion in this paper, using the term cohesion in a broad, macroscopic sense as any resistance to shearing in addition to friction. Due to the partially saturated state, the measured stresses do not exactly represent the effective stresses, but because of degree of saturation close to residual state they are assumed to be close to the effective stresses. However, the stresses and stress parameters, such as the friction angle, are written as effective parameters within this study. The additional shear strength in the moist specimens caused by suction induced effective stresses was approximated within the framework of unsaturated soil mechanics according to Vanapalli et al. [55] [Eq. 6], which is based on the fundamental definition of shear strength according to Fredlund et al. [13].

$$\tau = c' + (\sigma_n - u_a)\tan\varphi' + (u_a - u_w)\tan\varphi'\frac{S - S_r}{100 - S_r} \tag{6}$$

The cohesion is formulated similar to Rahardjo et al. [47] and Ling et al. [25] as the sum of effective cohesion c' and suction induced cohesion $(u_a - u_w)\tan\varphi'(S - S_r)/(100 - S_r)$. The matric suction $(u_a - u_w)$ for a given degree of saturation S and the degree of saturation at the beginning of the residual zone S_r were determined from the soil water characteristic curve (SWCC), which was calculated applying the model by Aubertin et al. [4]. As expected, the effect of suction on the shear strength is of minor importance within the range of the materials tested here with very low water contents. Cohesion in soil mechanics is usually determined as intercept of the Mohr–Coulomb failure envelope on the shear stress axis. Whereas it is possible to determine a convex failure envelope for dry sand in the $\tau - \sigma'$ space, because it is known that dry sand cannot carry any tension at zero stress, the situation is different with moist sand or even dry sand-clay mixtures. These materials have the capacity to stand vertically unsupported. Instead of a linearization of the Mohr-Coulomb envelope this capacity is used here to determine the cohesion

in centrifuge tests. Determination of cohesion is described by Mélix [36], who increased the vertical load on a laterally unsupported specimen mixed from sand, clay and water until failure was reached ($c = 0.5$–0.7 kPa). Mulugeta [39] presented the idea of increasing the vertical load by an increase in the acceleration in centrifuge tests in order to determine the cohesion of moist sand. Very recently, Shahnazari et al. [52] performed two centrifuge experiments on moist, slightly clayey, silty sand ($w = 5\,\%$; $c = 0.8$–0.9 kPa). We determined the cohesion for all mixtures used by this method within the geotechnical centrifuge. The working principle of centrifuge technology is described in Sect. 3.1.2. The specimens were placed between four surrounding walls by tamping to a predetermined density in several layers, then one wall was removed and the specimens stand vertically without any support on this side. The acceleration, and thus the stress level, was continuously increased until failure occurred, the point of failure was detected by image analysis. The acceleration is represented by a multiple of earth's gravity in the barycentre of the specimen, n, multiplied by earth's gravity. The acceleration at failure was used to determine the dominant effective stress level to enable the cohesion to be calculated. The shear stress in the failure plane, which was necessary in addition to friction to resist up to the gravity level at failure n_f, is called cohesion. The cohesion in this sense is calculated by applying the simple soil mechanical model of a sliding wedge. The forces acting at the slip wedge, weight of the specimen W in the increased gravity field, resulting friction Q and cohesion C, active earth pressure E_a and wall friction R, are marked in Fig. 3.

Setting up the horizontal and vertical equilibrium of forces and using the boundary condition of earth pressure E_a to be 0 on the unsupported side, the cohesion was determined by Eq. 7 according to Mulugeta [40], which is based on derivations by Jaeger and Cook [19].

$$c = \frac{\sigma_v}{2\tan(\theta)}. \tag{7}$$

Herein θ represents the slip angle with respect to the horizontal, calculated as $45° + \varphi'_p/2$. The peak friction angle φ'_p was determined in advance in a series of drained direct shear tests ($60 \times 60 \times 20$ mm, free upper frame) for all model materials used at vertical stresses between 10 kPa and 55 kPa. This corresponds to the range of vertical stress applied in the model experiments (1–60 kPa). Since the maximum principal stress σ_1 in the derivations by Jaeger and Cook [19] is a constant stress, whereas the vertical stress σ_v here is linearly increasing with depth, $\sigma_v = (\gamma h n)/2$ is inserted. γ is the specific weight under natural gravity, h the height of the slip wedge (= height of specimen). Wall friction between the specimen and the glass walls does not change the geometry of the slip wedge. Setting the wall friction angle equal to the internal friction angle, the calculated cohesion is slightly lower than without consideration of wall friction. In the present study the influence of wall friction on the value of cohesion determined is not more than 5 %. The reliability of these type of tests is checked by three variations for example of the loose ($1.40\ \mathrm{g/cm^3} \le \rho \le 1.44\ \mathrm{g/cm^3}$) $SC_{4\%}W_{1.7\%}$ mixtures. On the one hand, the boundary conditions were modified applying an additional surface load (3 tests), which was increased simultaneously to the weight of the specimen by acceleration in the geotechnical centrifuge. On the other hand, the geometry was modified by performing tests with a specimen's height of 10 cm (3 tests) and 7.5 cm (2 tests). The tests with the height of 7.5 cm were performed in a small model on the large geotechnical centrifuge (in a scale of 1:10), which is capable of testing specimens with a cohesion of $c \le 2$ kPa. The average value of the eight tests carried out in total results in a cohesion of 1.0 kPa, with a standard deviation of 0.3 kPa. Taking only the five tests without surface load into account, the cohesion is determined to be 1.2 kPa, with a standard deviation of 0.2 kPa. This method was applied to determine the cohesion for the material compositions listed in Table 3.

3 Model experiments

3.1 Methods

3.1.1 Experimental setup

The experimental series was performed in the modified "Bochum extensional device". This device was originally designed by Wolf et al. [68]. The specimen is placed on a rubber membrane, which is pulled to the right (Fig. 4). The homogeneous stretching of the membrane is supported by the scissors mechanism, which is constructed only to prevent transverse stretching of the membrane. The homogeneity of the strain field was controlled by Wolf et al. in natural (1 g) [69] and in increased (30 g) [66] gravity fields. The setup was recently modified for operating in acceleration fields up to 50 g. Besides, the pulling mechanism to apply the homogeneous strain field was reconstructed. Now, the membrane is directly pulled ($0.049\ \mathrm{mm/s} \mathrel{\hat{=}} \dot{\varepsilon} = 9 \cdot 10^{-5}\ /\mathrm{s}$) by massive clamps, the moveable wall is glued onto a thin part of the membrane to prevent pulling the wall away from the specimen.

The homogeneity was controlled after reconstructions in 1 g experiments by observation of the bottom side of the rubber membrane through a glass window by means of the DIC technique. The displacement u_x was determined at discrete positions x along a central and along a marginal line on the visible part of the membrane as shown in Fig. 5. The fitted linear function has an inclination of 0.106, which represents the value of the applied strain ε_{xx} at which the homogene-

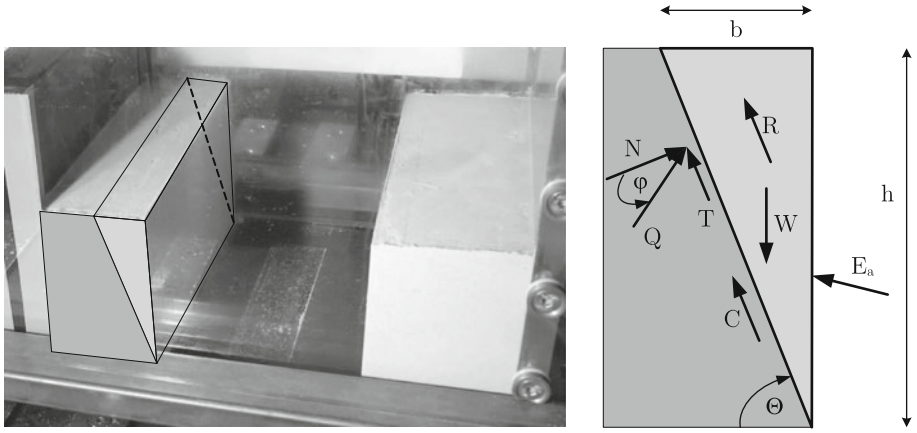

Fig. 3 Initial unsupported specimens with sketched slip wedge and forces acting at the slip wedge

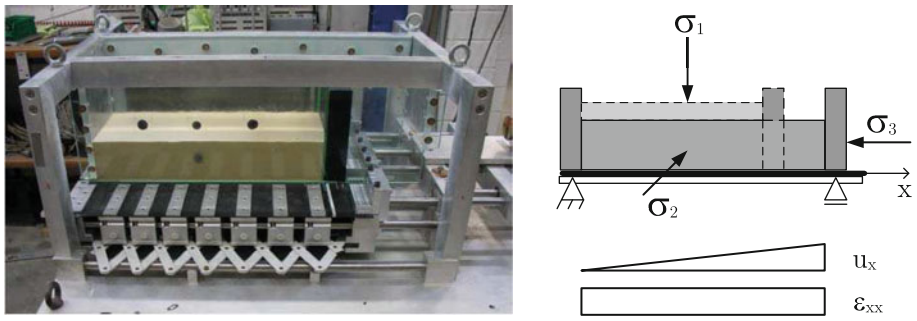

Fig. 4 The specimen is stretched homogeneously under plane strain boundary conditions in the "Bochum extensional device"

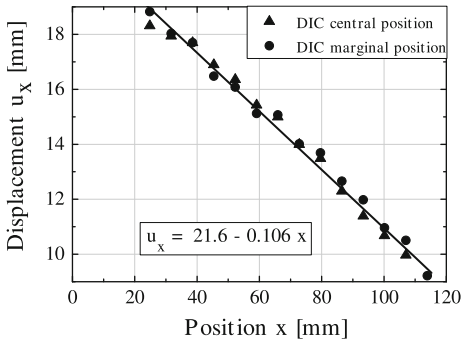

Fig. 5 Calculated displacement u_x in the pulling direction in the central and marginal part of the membrane (observed by the DIC method) confirms the homogeneous strain field

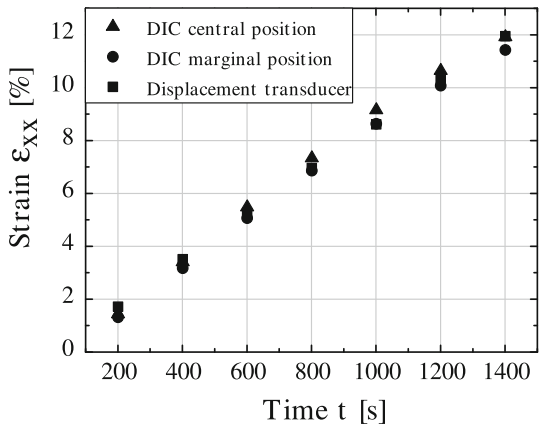

Fig. 6 Calculated strain ε_{xx} in pulling direction in the central and marginal part determined by the DIC corresponds to strain calculated from the measurement of displacement transducer

ity of the strain field is hereby confirmed. It is noteworthy that the strain, calculated by means of the DIC, corresponds to the strain measured by the displacement transducer (Fig. 6) during the complete experiment. The observation through the bottom window is not possible in centrifuge experiments. Therefore, the homogeneity was investigated in a 50 g experiment by the observation of the top side of aluminium bars with a total weight equivalent to the maximum specimen's weight used in the experimental program. If the distances between the aluminium bars are equidistant after having stretched the membrane by 10 %, then the homogeneous distribution of strain is ensured. The DIC method is not suitable in this case due to the gap appearing between the aluminium bars. However, no significant irregularities were noticed in the evaluation of the distances, measured in the shown digital image (Fig. 7).

3.1.2 Bochum geotechnical centrifuge

Since the investigation of failure in shear bands was intended to be studied in the model experiments, a sufficiently large vertical stress was required. Otherwise the specimen preferred failure in vertical tension cracks as a

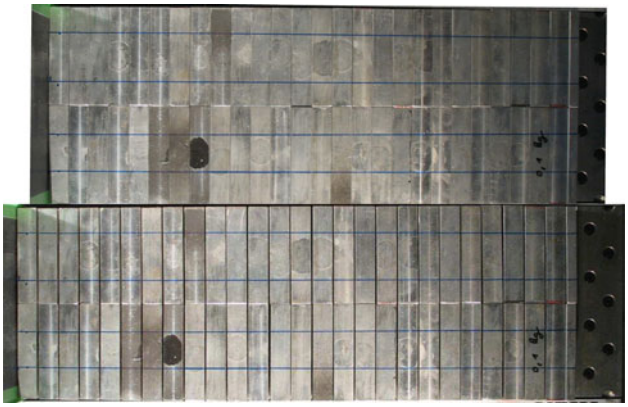

Fig. 7 View onto the aluminium bars before and after stretching the membrane by 10%. The homogeneity is confirmed by equidistance between the bars

consequence of their ability to stand vertically unsupported. Preliminary experiments revealed an upper bound in the ratio of cohesion related to the vertical stress in the magnitude of $c/\sigma_v = c/(\rho h g n) \leq 0.1$ to force shear failure. Since this condition cannot be fulfilled in the natural gravity field with the majority of the model materials (Table 3), most of the experiments were performed in the large Bochum Geotechnical Centrifuge. This beam centrifuge has a diameter of 8.25 m, for technical details see Jessberger and Güttler [21]. The experimental setup is positioned in one swinging basket. During the acceleration, the swinging basket rotates around its axes, such that the resulting force, composed by the vertical gravity force and the radial inertia force, acts normal to the base of the experimental setup, increasing the initial vertical stress in the specimen by the factor n.

3.1.3 Digital image correlation (DIC)

The DIC system was applied within the Bochum Geotechnical Centrifuge by implementing a real-time data acquisition system (Zornberg et al. [75]), which allows for the continuous observation of the specimen in the increased acceleration field up to 50 g. Glass side walls provide the in-plane observation of the specimen by two CCD compact cameras with a resolution of 1,280 × 1,024 pixels. By means of the DIC technique, it is possible to calculate the displacement and strain fields from a series of digital images. This technique was used by several authors for granular materials [1,42,44,49,62,65], a detailed description of the DIC system, as used, in 1 g experiments was given by Wolf et al. [68]. The digital images, taken with a frequency of 1 Hz, are transferred to a desktop computer, which is installed close to the rotating axis inside the centrifuge. Since the data acquisition needs large storage capacity, the recording is started just in time with the beginning of the experiment. A network has been installed via power line to control the computer inside the centrifuge via remote control software from a computer outside the centrifuge. The determination of all characteristics of a shear band system was realized, the onset of localization and the width of shear bands were determined as well as the spacing and the inclination at the onset of localization. Based on a series of digital images, the evaluation is performed by subdividing the area of interest into interrogation windows of a certain amount of pixels. The displacement vector between time t and $t + \Delta t$ is calculated by the gray value intensity of the pixel structure via a cross correlation algorithm. The calculation typically was performed with a multipass process with an initial window size of 32 × 32 pixels and a final size of 8 × 8 pixels. Locking effects, as described by Nübel and Weitbrecht [42], were prevented, since one grain of d_{50} size is represented by at least 1 pixel. By applying an overlap of the interrogation windows of 50 % in both directions, the spatial resolution was increased, one vector represented the displacement of a group of 4 × 4 pixels. Since the calibration typically produces a factor of 4 pixels/mm, one vector represented a group of 1 × 1 mm or 4 × 4 grains, i.e. the displacement of a group of 16 grains in total. Thus, the minimum number of particles, as defined by Raffel [46] as being necessary for precise results, was maintained. The shear strain field is calculated as $\gamma = \epsilon_1 - \epsilon_3$ as a derivative from the displacement vector field. As an example we refer to Figs. 13 and 14 where the scalar value of shear strain along an horizontal line is plotted in a profile. Each local maximum, exceeding a certain threshold value of shear strain γ, was defined as a zone of localization of shear deformation, i.e. a shear band.

3.2 Results: shear band geometry

The observation of the localization process revealed noticeable differences, depending on the materials used. In dry, dense Silversand, the shear bands could hardly be noticed by visual observation through the glass walls within the applied strain range, although they were visible on the top surface. However, the shear bands could be identified by means of the DIC method. The shear bands could not be detected by means of the DIC method in the experiments with moist sand. Inserting several layers of black colored Silversand obviously improved the identification of failure planes (Fig. 8). Like in dry sand, the simple shear deformation mode within the shear band can be observed, whereby a kink in the displacement field (weak discontinuity) is characteristic. On the contrary, adding small amounts of Kaolin clay to the Silversand, the failure zones can easily be observed by eye. The shear bands appear to be very clear discontinuity faults, i.e. with a jump in the displacement field (Fig. 9). Similarly, in the mixtures composed of Silversand, Kaolin clay and water, the failure zones appear rather as strong discontinuity zones. Desiccation cracks were observed on the top surface in

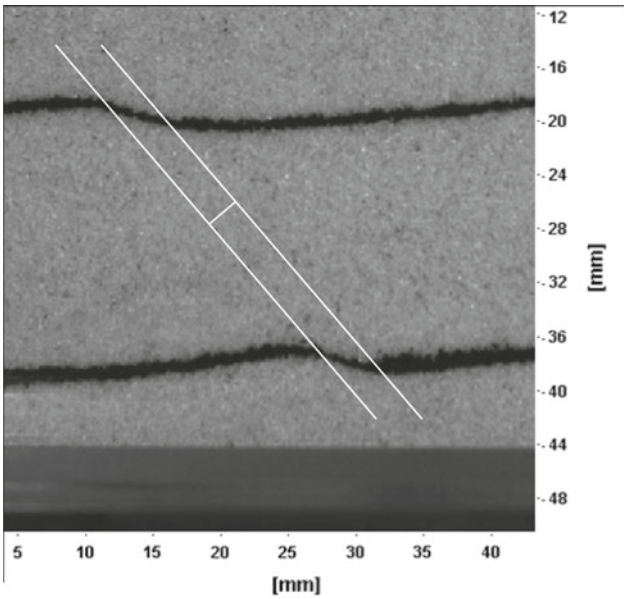

Fig. 8 Thick failure zone of 11 d_{50} in material composition $SW_{1\%}$

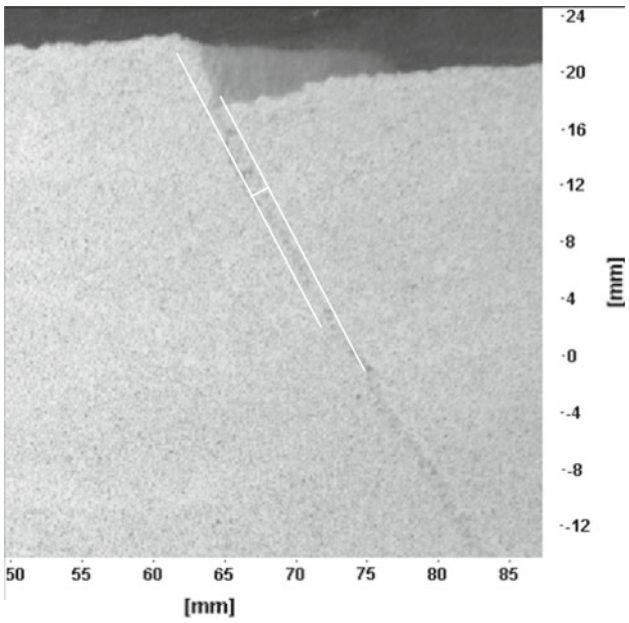

Fig. 9 Thin failure zone of 5 d_{50} in material composition $SC_{20\%}$

these compositions, where the shear failure started to develop downwards. In all other materials, the shear bands appeared simultaneously over the specimen's height. Some conjugated shear bands developed, but still one preferred direction of shear band orientation dominated. A further difference, compared to dry sand, was observed in terms of the progression of the failure zones. The shear bands did not appear simultaneously in the material mixtures as in dry sand, and a systematic development, e.g. consecutive shear bands starting from the pulling side, was not observed.

3.2.1 Shear band inclination θ

The inclination θ was determined for each shear band with respect to the horizontal at the onset of its localization, based on the DIC evaluation (Fig. 10). These measured values are compared with the solutions according to Roscoe θ_R, Coulomb θ_C and Arthur θ_A, defined by Eqs. 1–3. The peak friction angle φ'_p, and the dilation angle ψ_p at the peak friction angle, were determined in biaxial extension tests (Sect. 4). The inclinations were found to lie in the range between the lower and the intermediate bound. Only the inclination in mixture $SC_{4\%}W_{1.7\%}$, md was found to lie between the intermediate and the upper bound.

3.2.2 Shear band thickness d_B

The shear band thickness d_B was determined by means of the DIC method according to the procedure introduced by Nübel [41], and adopted by Wolf et al. [68]. The strain distribution inside the shear band is assumed to follow a normal or a Gaußian distribution. The shear band thickness is calculated as twice the standard deviation of the distribution function, $d_B = 2\sigma$. The shear band thickness in the materials used was found to be in the range of 5–11 d_{50} (Fig. 11) by applying this procedure.

These values are in accordance with the values of shear band thickness measured in scaled digital images, in cases when they were clearly visible. The minimum thickness (5 d_{50}) was observed in mixture $SC_{20\%}$ (Fig. 9), the maximum thickness (11 d_{50}) in mixture $SW_{1\%}$ (Fig. 8). The figures show a thin failure zone in the strong discontinuity mode (Fig. 9) and a thick failure zone in the weak discontinuity mode (Fig. 8). It is noteworthy that the minimum thickness was observed in the material with the largest coefficient of uniformity ($SC_{20\%}$, $C_U = 48.9$), whereas a larger thickness was observed in the materials with a smaller coefficient of uniformity (e.g. Silversand, $C_U = 1.8$). On the other hand, the difference in the thickness, e.g. between $SC_{20\%}$ and Silversand, is not very large (5 d_{50} in comparison with 7 d_{50}), whereas the coefficient of uniformity is very different.

3.2.3 Shear band spacing a

The spacing a was determined as the horizontal distance between the neighbouring peaks in the shear strain profile calculated by the DIC method. Since the spacing in granular materials linearly depends on the height of the specimen (e.g. Wolf et al. [68]), the horizontal spacing a is normalized by the height h' of the specimen at the onset of localization, which assumes homogeneous deformation before the onset of localization.

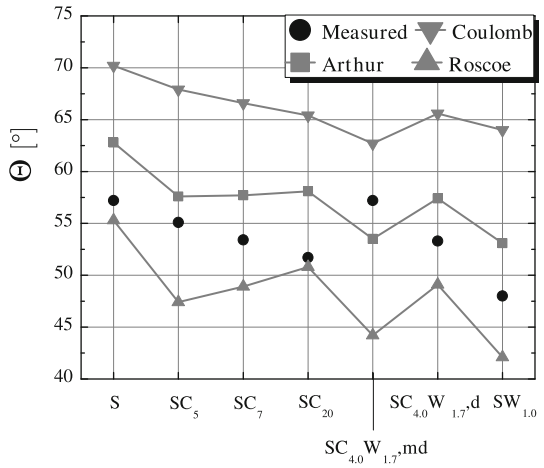

Fig. 10 The measured inclination of shear bands (average value) at the onset of localization in comparison with the theoretical solutions by Roscoe, Coulomb and Arthur

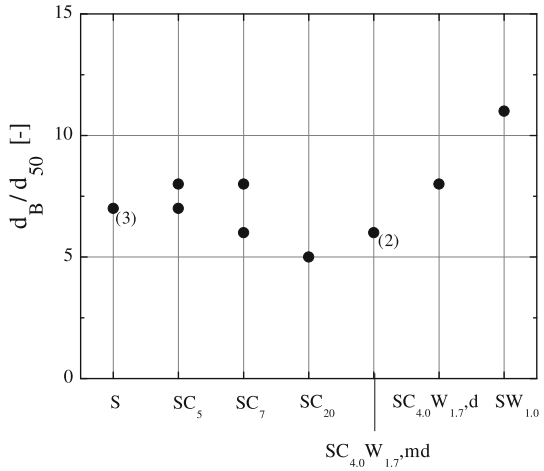

Fig. 11 The normalized shear band thickness in the material compositions used is found to be in the range of 5–11 d_{50}. Numbers in brackets indicate number of experiments evaluated, when identical experiments have been performed with the same results

The normalized spacing a/h' was determined to lie in a range of 0.23 for dry, dense sand to 0.56 for the moist, medium dense sand-clay composition $SC_{4\%}W_{1.7\%}, md$ (Fig. 12). The resulting shear band system of this moist sand-clay mixture is shown in Fig. 13, below a shear band system in the dry sand-clay mixture $SC_{7\%}$ (Fig. 14).

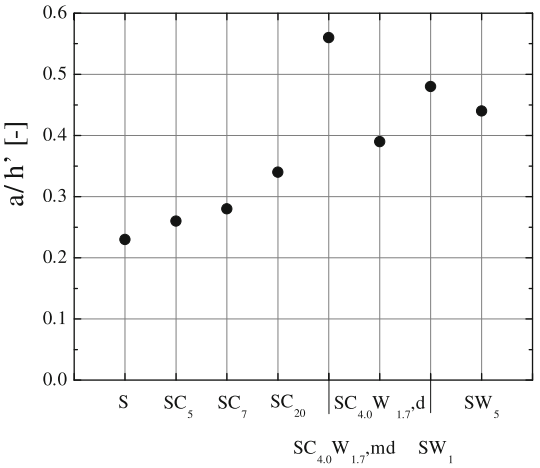

Fig. 12 Normalized shear band spacing a/h' for the materials tested

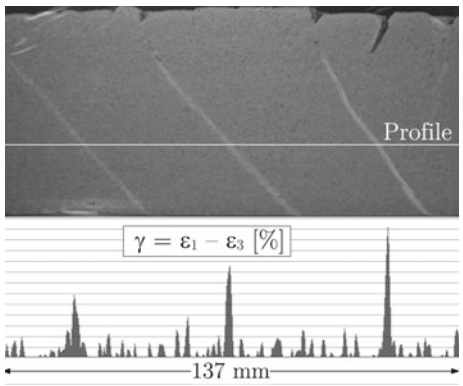

Fig. 13 Shear band system in $SC_{4\%}W_{1.7\%}, md$ mixture, $h = 0.10$ m, 25 g

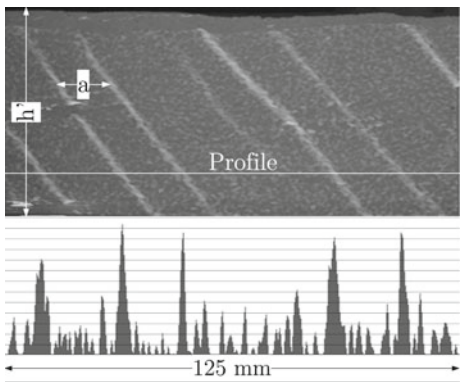

Fig. 14 Shear band system in $SC_{7\%}$ mixture, $h = 0.10$ m, 18 g

4 Plane strain compression and extension tests

4.1 Plane strain device

The newly designed biaxial device (Fig. 15) consists of an opposing pair of rigid walls to ensure plane strain conditions and an opposing pair of flexible walls to permit free shear band formation in simple shear mode. The flexible walls are constructed as water cushions, in which the water pressure is controlled via software and a pressure control valve up to 300 kPa.

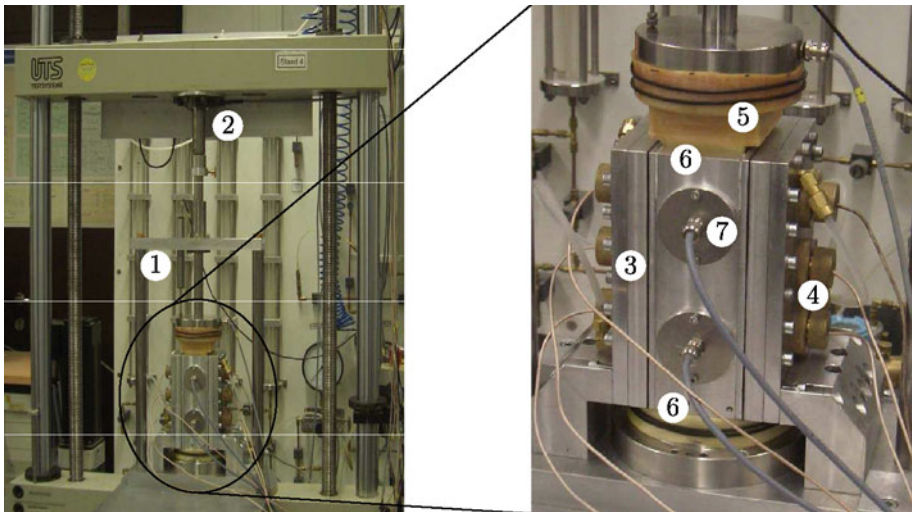

Fig. 15 *1* Displacement transducer measuring vertical deformation. *2* Load cell measuring vertical force. *3* Water cushion as flexible wall. *4* Three contact free displacement sensors installed within each water cushion for horizontal deformation measurement. *5* Preformed latex membrane wrapping the $60 \times 80 \times 130$ mm specimen. *6* Vertical pressure transducer in top and bottom end plate. *7* Pressure transducer integrated in one rigid wall, measuring the intermediate stress σ_2'

The horizontal stress is measured by pressure transducers in two positions in one rigid wall. The horizontal deformation is measured locally by six contact free displacement sensors, which are integrated into the water cushions. The vertical pressure is determined redundantly by a load cell measuring the vertical force outside the biaxial cell and by pressure transducers in the top and bottom end plates.

4.2 Plane strain extension tests

A series of plane strain extension tests was performed at three different horizontal initial stresses $\sigma_1' = 78, 175, 300$ kPa. The dry sand specimens were prepared by air pluviation, whereas the material mixtures were prepared by tamping in several layers of maximum 30 mm depth to a predetermined density. Friction at the end plates was reduced by a layer of silicon grease and a latex membrane. The preformed latex membrane exactly surrounding the specimen of rectangular cross section area was lubricated with silicon grease. Vacuum of 20 kPa was applied to keep the specimen in position before installing the rigid and flexible side walls. The biaxial extension tests were performed along the stress path presented in Fig. 16. In phase A, the horizontal stress σ_1' inside the water cushions was increased while the strains ε_2 (normal to the rigid wall) and ε_3 (vertical) were kept zero (K_0 stress path). In phase B, σ_1' and ε_2 were kept constant while the vertical stress was reduced displacement controlled (0.002 mm/s $\hat{=}$ $1.5 \cdot 10^{-5}$ /s).

A comparison of plane strain and triaxial extension with medium sand of different initial densities reveals that the peak friction angle is larger in plane strain extension (Fig. 17). The difference is greater in dense sand than in loose sand, as was observed by Schanz and Vermeer [51] in a comparison of plane strain and triaxial compression. In plane strain extension, the critical, isochoric state is reached at smaller

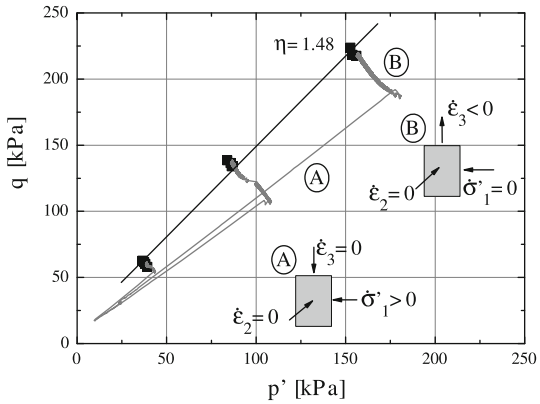

Fig. 16 Stress path of biaxial extension tests for a dry sand-clay mixture ($SC_{7\%}$). $p' = (\sigma_1' + \sigma_2' + \sigma_3')/3$, $q = \sqrt{(\sigma_1' - \sigma_2')^2 + (\sigma_2' - \sigma_3')^2 + (\sigma_1' - \sigma_3')^2}/\sqrt{2}$

shear strain, which can be deduced from the measurement of the volumetric strain (Fig. 18). In triaxial extension a larger value of absolute volumetric strain was observed, which is in agreement with results by Green [14].

Results of biaxial extension tests with $\sigma_1' = 78$ kPa are presented in Figs. 19 and 20. The friction angle in dense sand increases to a maximum value, followed by strain softening, whereas the friction angle in loose sand continuously increases. The same tendency was observed with a moist sand-clay mixture $SC_{4\%}W_{1.7\%}$ of different densities. This expected behaviour was accompanied by dilation of the dense materials and contraction in loose to medium dense materials.

4.3 Strain softening gradient k

All existing analytical approaches mentioned in Sect. 1.2 contain the strain softening gradient as a crucial parame-

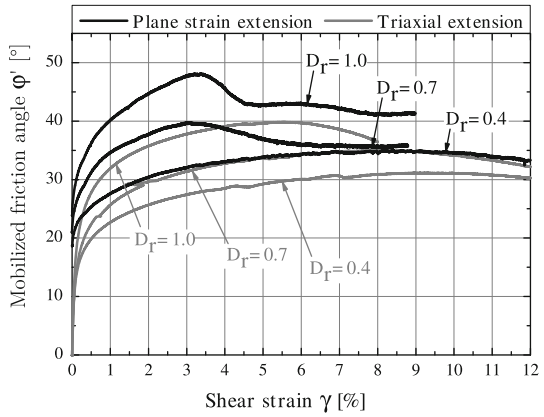

Fig. 17 Comparison of biaxial and triaxial extension tests with different initial densities. Medium sand: 0.1 mm $\leq d \leq$ 0.71 mm, d_{50} = 0.35 mm, $C_U = 1.5$, $e_{max} = 0.79$, $e_{min} = 0.50$, $\sigma_1' = 175$ kPa, triaxial tests by Wolf et al. [69]

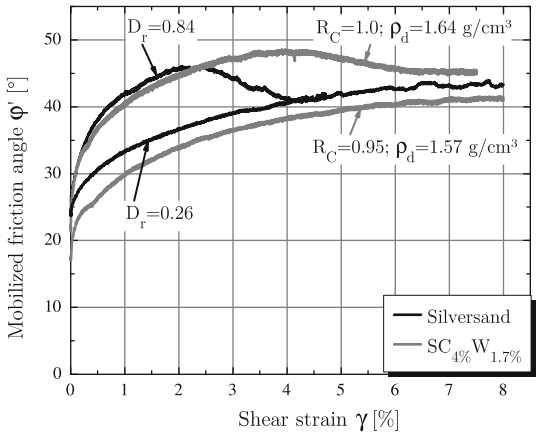

Fig. 19 Biaxial extension tests, $\sigma_1' = \sigma_h' = 78$ kPa $= const$. The most pronounced softening is observed in dense sand, no softening is observed in loose sand and medium dense $SC_{4\%}W_{1.7\%}$, md mixture

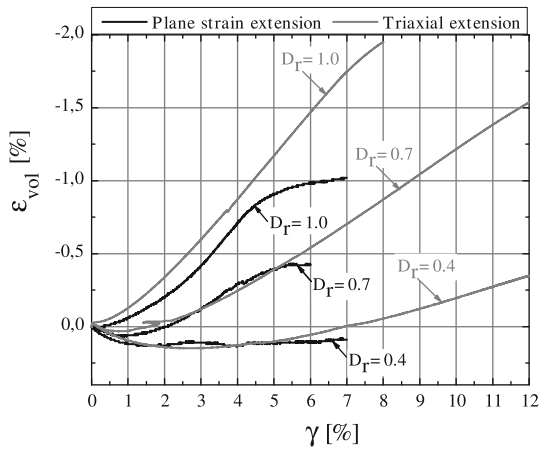

Fig. 18 Comparison of biaxial and triaxial extension tests with different initial densities in medium sand. Volumetric strain versus shear strain

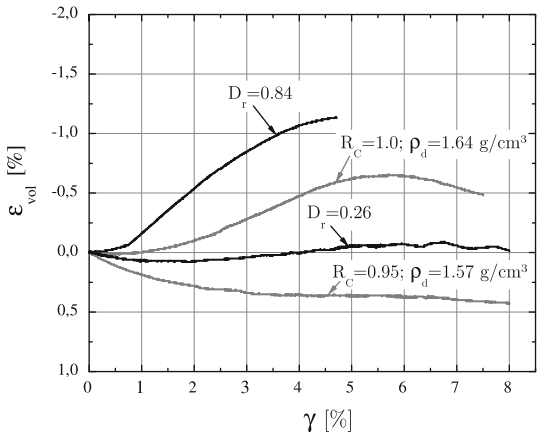

Fig. 20 Biaxial extension tests, $\sigma_1' = \sigma_h' = 78$ kPa $= const$. The largest dilation is observed in dense sand, no dilation is observed in loose sand and medium dense $SC_{4\%}W_{1.7\%}$, md mixture

ter explaining the shear band spacing in a system of parallel shear bands. The strain softening gradient was assumed to be constant between the peak and the critical value by Leśniewska and Wolf and also others (e.g. Marcher [28]), although Wolf [66] assumed this to be a rough approximation. The strain softening gradient k may also be determined in a small range immediately after the peak, but each chosen range would be arbitrary. Therefore, k was defined in this paper as the maximum change of the friction angle φ' with ongoing shearing γ in the softening regime, $k = |\Delta\varphi'/\Delta\gamma|_{max}$. It is noteworthy that the softening was calculated as a derivative of φ' with respect to γ, although the shear strength of the materials used is composed of frictional and (apparent) cohesive strength. However, φ' is used as a stress parameter to express the current shear stress state, as proposed by Hayano et al. [17] Softening was accompanied by shear banding in the majority of the biaxial compression tests. The shear bands were observed after the experiments. The occurrence of banding softening, instead of material softening, was confirmed according to Wanatowski and Chu [61] by simultaneous maxima of q and q/p'. The softening inside the shear band can be determined by local measurement of deformation, as carried out e.g. by Hayano et al. [17]. In our experiments, the contact free displacement sensors (CFDS's) were arranged in a way that the developing shear band in biaxial compression tests is located between at least one pair of displacement sensors (CFDS 3 and CFDS 4 in Fig. 1). Therefore, the horizontal deformation inside the shear band could be calculated, neglecting elastic deformation outside the shear band after the onset of localization. The shear bands do not perfectly pass between two CFDS's in biaxial exten-

sion tests, since they are inclined at a small angle with respect to the horizontal. Furthermore, a conjugated pair of crossing shear bands appeared in most tests. Thus, in biaxial extension tests, strain softening was determined in the whole specimen. Therefore, the relationship between the strain softening inside the shear band, k_B, and that of the whole specimen, k, was studied in biaxial compression tests. The relationship was assumed to be the same in biaxial extension. Analyzing the relation between k and k_B, the rate of shear strain in the whole specimen γ and inside the shear band γ_B are calculated according to Eqs. 8 and 9, respectively.

$$\gamma = \varepsilon_1 - \varepsilon_3 = -\ln\left(\frac{h_0 - \Delta h(t)}{h_0}\right) + \ln\left(\frac{w_0 - \Delta w(t)}{w_0}\right) \quad (8)$$

$$\gamma_B = \frac{u_{x'}}{d_B} = \frac{u_v(t)\sin(\theta_B) + u_h(t)\cos(\theta_B)}{d_B} \quad (9)$$

$\Delta h(t)$ is the change of the specimen's height, $\Delta h(t) \geq 0$ in compression, compared to the initial height h_0. $\Delta w(t)$ is the change of the specimen's width, $\Delta w(t) \leq 0$ in compression, as difference to the initial width w_0. Neglecting elastic deformations and bedding errors, $\Delta h(t) = u_v(t)$. $\Delta w(t)$ is calculated as average of all three pairs of CFDS's, whereas u_h according to Fig. 1 is the difference between CFDS 3 and CFDS 4. The equality of $\Delta w(t) = -u_h(t)$ is exactly fulfilled only if the shear band passes between all three pairs of CFDS's, but the experiments indicate that this equality can be used as a good approximation. The inclination θ_B and the thickness d_B of the shear band are assumed to be constant in the softening regime. The time derivatives of the shear strains, or incremental shear strains, respectively, are then as follows:

$$\dot{\gamma} = \frac{\partial \Delta h(t)/\partial t}{h_0 - \Delta h(t)} - \frac{\partial \Delta w(t)/\partial t}{w_0 - \Delta w(t)} \triangleq \frac{(\Delta u_v/\Delta t)}{h_0 - (\Delta u_v/\Delta t)t} + \frac{(\Delta u_h/\Delta t)}{w_0 + (\Delta u_h/\Delta t)t} \quad (10)$$

$$\dot{\gamma}_B = \frac{\partial u_v/\partial t \sin(\theta_B) + \partial u_h/\partial t \cos(\theta_B)}{d_B} \triangleq \frac{(\Delta u_v/\Delta t)\sin(\theta_B)}{d_B} + \frac{(\Delta u_h/\Delta t)\cos(\theta_B)}{d_B} \quad (11)$$

The change in the specimen's width $(\Delta u_h/\Delta t)$ is approximated to be constant after the peak, as confirmed from experimental results. $\Delta\gamma_B/\Delta\gamma$ was then calculated to be almost constant during the softening regime. As a consequence, the relation between the softening gradients k/k_B remains constant after the peak. However, this constant value obviously depends on the initial specimen geometry in terms of h_0 and w_0, as well as on the grain size distribution curve in terms of d_{50}, which determines the thickness of the shear band d_B. So far, the results are in accordance with Tatsuoka et al. [54], who calculated a more pronounced softening with increasing initial height and with Yoshida et al. [74], who found a unique softening inside the shear band independent of d_{50}, which results to a more pronounced softening of the specimen with decreasing d_{50} [54]. For the example of a dense sand specimen, the calculation is performed by inserting the following parameters: $h_0 = 135$ mm, $w_0 = 60$ mm, $\Delta u_v/\Delta t = 2 \cdot 10^{-3}$ mm/s, $\Delta u_h/\Delta t = 1.1 \cdot 10^{-3}$ mm/s, $\theta_B = 68\,°$, $d_B = 7.8$ mm. The value $\Delta\gamma_B/\Delta\gamma = k/k_B$ was calculated to be 8.8. Now, the shear strain inside the band γ_B is divided by 8.8, shown as γ calculated from γ_B in Fig. 21. This calculated function fits very well to the measured curve. It is noteworthy that the shear strain inside the shear band is calculated as $\gamma_B = \gamma_{peak} + u_{x'}/d_B$ according to Yoshida et al. [74], assuming homogeneous deformation in the pre-peak regime. The procedure was tested successfully with materials of different softening gradients. Thus, the strain softening gradient of the whole specimen, with γ determined by local displacement measurement, can be seen as a characteristic property of the material tested in plane strain compression with identical initial geometry and mean grain size. The same was assumed to be valid in biaxial extension.

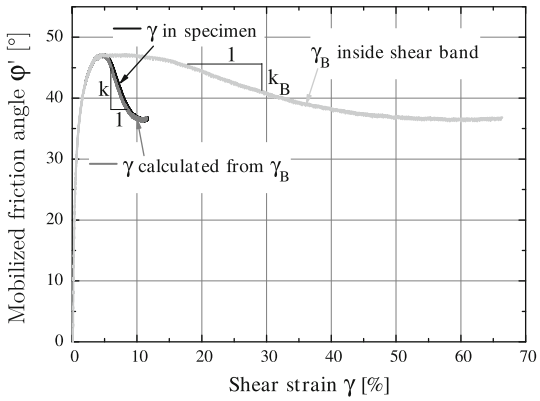

Fig. 21 Functions of mobilized friction angle with ongoing shearing. Comparison of shear strain γ in the whole specimen and γ_B inside shear band. Shear strain γ calculated from γ_B is in good agreement with measured γ

In biaxial extension tests, it was observed that a larger strain softening gradient k is accompanied by a larger dilation angle ψ_p (Fig. 22). The dilation angle ψ for the whole specimen is calculated according to Eq. 12, whereas the local dilation angle inside the shear band ψ_B (Fig. 1) is defined in Eq. 13. As shown recently by Gutierrez and Vardoulakis [15], both formulations result in a similar value.

$$\psi = \arcsin\left(\frac{\dot{\varepsilon}_v}{\dot{\gamma}}\right) \quad (12)$$

$$\psi_B = \theta - \arctan\left(\frac{\Delta u_v}{\Delta u_h}\right) \quad (13)$$

Contrary to this general tendency, the mixture $SC_{20\%}$ showed strong softening behaviour accompanied by a smaller dilation than dense sand. This is even more pronounced in the case of pure Kaolin clay, which gives reason to the assump-

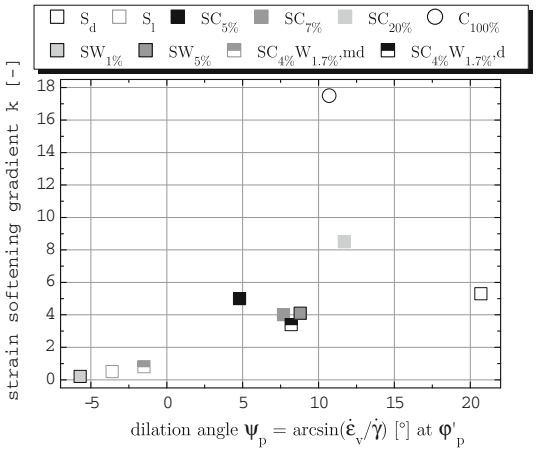

Fig. 22 Relationship between global strain softening gradient k and global dilation angle ψ in biaxial extension tests with $\sigma_1' = \sigma_h' = 78$ kPa $= const.$

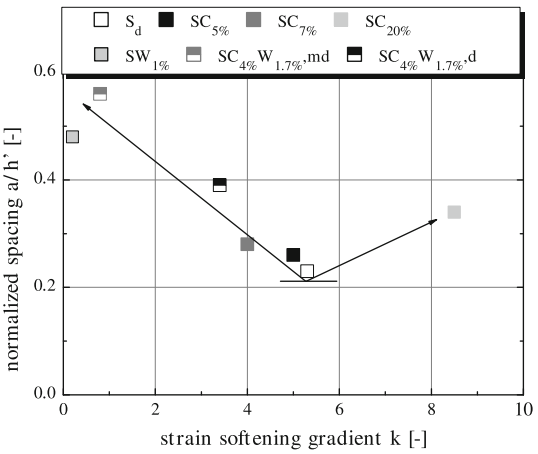

Fig. 23 The normalized shear band spacing a/h' increases with decreasing strain softening gradient k in the majority of the model materials

tion that strong softening associated with small dilation is a response of the failure characteristics inside the shear band dominated by the clay particles.

4.4 Results: strain softening and shear band spacing

The combination of the results from model experiments and from biaxial tests now reveal that the normalized shear band spacing a/h' increases in general with decreasing softening gradient k (Fig. 23). This experimental observation confirms the model of Wolf and contradicts those of Leśniewska and Mandl. It is remarkable that the observations concerning the mixture $SC_{20\%}$ do not agree with this general tendency, since the normalized shear band spacing in the model experiment was 0.34, which is larger than expected considering the large softening gradient of 8.5. Regarding the dry, dense sand as a reference material, mixture $SC_{20\%}$ is the only one for which the idea of increasing spacing with increasing softening gradient was observed. The failure mode in this case resembles rather the strong discontinuity mode, which corresponds to the assumed mode by Leśniewska and Mandl, whereas Wolf was exclusively concerned with the weak discontinuity mode.

However, the dry sand represents a lower bound of shear band spacing within the broad range of materials tested.

5 Conclusions

The geometry and spatial distribution of shear failure zones in a broad range of model materials was investigated in plane strain model experiments under extensional loading. Different material mixtures were investigated, composed by varying portions of Silversand, Kaolin clay and water. Most of the experiments were performed in the "Bochum Geotechnical Centrifuge", because the vertical stress in the specimen needs to be at least an order of magnitude larger than the cohesion of the material mixtures in order to force shear failure to occur. The cohesion, defined as the sum of all components of shear resistance in addition to friction, was determined in centrifuge experiments by accelerating a vertically unsupported specimen until failure occured. Shear bands in the model experiments were detected by means of the digital image correlation (DIC) technique within the "Bochum Geotechnical Centrifuge" and the homogeneity of the induced strain field was ensured up to 50 g. The inclinations of the shear bands at the onset of localization were found to occur between the solution according to Roscoe and the solution according to Arthur, and the thickness was determined to be in the range of 5–11 d_{50}. The shear bands appear more easily defined if clay was added and less clear if water was added. The spacing between two adjacent shear bands within the system of parallel shear bands increased with the addition of clay and/or water, dry sand representing a lower bound. The stress-strain behaviour of the materials was investigated in a new plane strain device, which is capable of performing biaxial compression and extension tests. The strain softening gradient was determined for the whole specimen as well as inside the shear band (in biaxial compression), showing an almost constant relation between them. Furthermore, the combination of the results from model experiments and biaxial tests under extensional loading revealed an increasing shear band spacing with decreasing strain softening gradient. The aspects of strain softening, dilatancy, shear band spacing, mode of discontinuity and width of the failure zone were studied for the mixture $SC_{20\%}$. The results differ from the general tendencies, supporting the assumption that mixtures with a large content of clay resemble, more than the other materials used in this study, normal fault characteristics in rock formations.

Acknowledgments The research was supported by the German Research Foundation (Deutsche Forschungsgemeinschaft, DFG) in the frame of the Collaborative Research Center (SFB) 526 "Rheology of the Earth". This support is gratefully acknowledged by the authors.

References

1. Adam, J., Urai, J., Wieneke, B., Oncken, O., Pfeiffer, K., Kukowski, N., ad Lohrmann, J., Hoth, S., van der Zee, W., Schmatz, J.: Shear localisation and strain distribution during tectonic faulting—new insights from granular-flow experiments and high-resolution optical image correlation techniques. J. Struct. Geol. **27**, 283–301 (2005)
2. Alshibli, K.A., Batiste, S.N., Sture, S.: Strain localization in sand: plane strain versus triaxial compression. J. Geotech. Geoenviron. Eng. **129**(6), 483–494 (2003)
3. Arthur, J.R.F., Dunstan, T., Al-Ani, Q.A.J.L., Assadi, A.: Plastic deformation and failure in granular media. Géotechnique **27**(1), 53–74 (1977)
4. Aubertin, M., Mbonimpa, M., Bussière, B., Chapuis, R.: A model to predict the water retention curve from basic geotechnical properties. Can. Geotech. J. **40**, 1104–1122 (2003)
5. Brun, J.P. : Deformation of the continental lithosphere: insights from brittle-ductile models. In: De Meer, S., Drury, M., De Bresser, J., Pennock, G. (eds.) Deformation Mechanism, Rheology and Tectonics: Current Status and Future Perspectives, pp. 355–370. Geological Society, London (Special Publications, 200) (2002)
6. Cloos, E.: Experimental analysis of gulf coast fracture patterns. AAPG **52**(3), 420–444 (1968)
7. Cloos, H.: Über Biegungsbrüche und selektive Zerlegung. Int. J. Earth Sci. **24**(3–4), 203–219 (1933)
8. Coulomb, C.: Essai sur une application des régules des maximis et minimis à quelques problèmes de statique rélatifs à architecture. Mém. Divers. Savants **7**, 343–382 (1776)
9. Cundall, P.: Numerical modelling of jointed and faulted rock. In: Rossmanith, H.-P. (ed.) Mechanics of Jointed and Faulted Rock, pp. 11–18. Balkema, Rotterdam (1990)
10. Desrues, J., Viggiani, G.: Strain localization in sand: an overview of the experimental results obtained in Grenoble using stereophotogrammetry. Int. J. Num. Anal. Meth. Geomech. **28**, 279–321 (2004)
11. Drescher, A., Vardoulakis, I., Han, C.: A biaxial apparatus for testing soils. Geotech. Test. J. ASTM **13**(3), 226–234 (1990)
12. Exdaktylos, G., Vardoulakis, I., Stavropoulou, M., Tsombos, P.: Analogue and numerical modeling of normal fault patterns produced due to slip along a detachment zone. Tectonophysics **376**, 117–134 (2003)
13. Fredlund, D., Morgenstern, N., Widger, R.: The shear strength of unsaturated soils. Can. Geotech. J. **15**(3), 313–321 (1978)
14. Green, G.: Strength and deformation of sand measured in an independent stress control cell. In: Proceedings of the Roscoe Memorial Symposium on Stress-Strain Behaviour of Soils, pp. 285–323. Cambridge (1971)
15. Gutierrez, M., Vardoulakis, I.: Energy dissipation and post-bifurcation behaviour of granular soils. Int. J. Numer. Anal. Methods Geomech. **31**, 435–455 (2007)
16. Harper, T., Fossen, H., Hesthammer, J.: Influence of uniform basement extension on faulting in cover sediments. J. Struct. Geol. **23**, 593–600 (2001)
17. Hayano, K., Maeshiro, T., Tatsuoka, F., Sato, T., Wang, L., Kodaka, T.: Shear banding in a sedimentary soft mudstone subjected to plane strain compression. Geotech. Test. J. **22**, 67–79 (1999)
18. Ishikawa, M., Otsuki, K.: Effects of strain gradients on asymmetry of experimental normal fault systems. J. Struct. Geol. **17**(7), 1047–1053 (1995)
19. Jaeger, J., Cook, N.: Fundamentals of rock mechanics. Chapman and Hall Ltd, London (1971)
20. Jeng, F.S., Lu, C.Y., Lee, C.L. : Major scale effects influencing model simulation of neotectonics. In: Kimura, T., Kusakabe, O., Takemura, J. (eds.) Centrifuge 98, pp. 911–916. Balkema, Rotterdam (1998)
21. Jessberger, H., Güttler, U.: Bochum geotechnical centrifuge. In: Corté, J. (ed.) Proceedings of International Conference on Geotechnical Centrifuge Modell. Centrifuge '88, Paris, pp. 37–44. Balkema, Rotterdam (1988)
22. Lade, P., Duncan, J.: Cubical triaxial tests on cohesionless soil. J. Soil Mech. Found. Div. ASCE **99**(SM10), 793–811 (1973)
23. Leśniewska, D.: Analysis of Shear Band Pattern Formation in Soil. Institute of Hydro-Engineering of the Polish Academy of Sciences (IBW PAN), Gdańsk (2000)
24. Leśniewska, D., Mróz, Z.: Study of evolution of shear band systems in sand retained by flexible wall. Int. J. Numer. Anal. Methods Geomech. **25**, 909–932 (2001)
25. Ling, H., Wu, M.H., Leshchinsky, D., Leshchinsky, B.: Centrifuge modeling of slope instability. J. Geotech. Geoenviron. Eng. **135**(6), 758–767 (2009)
26. Mandl, G.: Faulting in Brittle Rocks. Springer, Berlin (2000)
27. Marachi, N., Duncan, J., Chan, C., Seed, H. : Plane-strain testing of sand. In: Young, R., Townsend, F. (eds.) Laboratory Shear Strength of Soil, pp. 294–302. American Society for Testing and Materials, USA (1981)
28. Marcher, T.: Nichtlokale Modellierung der Entfestigung dichter Sande und steifer Tone. Ph.D. thesis, Institut für Geotechnik der Universität Stuttgart, Mitteilung 50 (2002)
29. Masuda, T., Tatsuoka, F., Yamada, S., Sato, T.: Stress-strain behavior of sand in plane strain compression, extension and cyclic loading tests. Soils Found. **39**(5), 31–45 (1999)
30. McClay, K.: Deformation mechanics in analogue models of extensional fault systems. Geol. Soc. Spec. Publ. **54**, 445–453 (1990)
31. McClay, K., Ellis, P.: Geometries of extensional fault systems developed in model experiments. Geology **15**, 341–344 (1987)
32. McIntosh, K., Silver, E., Shipley, T.: Evidence and mechanisms for forearc extension at the accretionary Costa Rica convergent margin. Tectonics **12**(6), 1380–1392 (1993)
33. Mühlhaus, H.B., Vardoulakis, I.: The thickness of shear bands in granular materials. Géotechnique **37**(3), 271–283 (1987)
34. Milligan, G.: The behaviour of rigid and flexible retaining walls in sand. Ph.D. thesis, University of Cambridge (1974)
35. Mitchell, J., Soga, K.: Fundamentals of Soil Behavior. Wiley, New York (2005)
36. Mélix, P.: Modellversuche und Berechnungen zur Standsicherheit oberflächennaher Tunnel. Ph.D. thesis, Institut für Bodenmechanik und Felsmechanik der Universität Fridericiana in Karlsruhe, Gudehus, G., Natau, O. (eds.) (1987). Heft 103
37. Morellato, C., Redini, F., Doglioni, C.: On the number and spacing of faults. Terra. Nova. **15**(5), 315–321 (2003)
38. Muir Wood, D.: Some observations of volumetric instabilities in soils. Int. J. Solids Struct. **39**, 3429–3449 (2002)
39. Mulugeta, G.: Modelling the geometry of Coulomb thrust wedges. J. Struct. Geol. **10**(8), 847–859 (1988)
40. Mulugeta, G.: Squeeze box in a centrifuge. Tectonophysics **148**, 323–335 (1988)
41. Nübel, K.: Experimental and numerical investigation of shear localization in granular material. Ph.D. thesis, Institut für Bodenmech-

anik und Felsmechanik der Universität Fridericiana in Karlsruhe (2002). Heft 159
42. Nübel, K., Weitbrecht, V.: Visualization and localization in grain skeletons with particle image velocimetry. J. Test. Eval. **30**(4), 322–329 (2002)
43. Oda, M., Kazama, H.: Microstructure of shear bands and its relation to the mechanisms of dilatancy and failure of dense granular soils. Géotechnique **484**, 465–481 (1998)
44. Paikowsky, S., Xi, F.: Particle motion tracking utilizing a high-resolution digital ccd camera. Geotech. Test. J. **23**(1), 123–134 (2000)
45. Peters, J., Lade, P., Bro, A. : Shear band formation in triaxial and plane strain tests. In: Donaghe, R., Chaney, R., Silver, M. (eds.) Advanced Triaxial Testing of Soil and Rock, pp. 604–627. American Society for Testing and Materials, Philadelphia (1988)
46. Raffel, M., Willert, C., Kompenhans, J.: Particle Image Velocimetry. Springer, Berlin (1998)
47. Rahardjo, H., Lim, T., Chang, M., Fredlund, D.: Shear strength characteristics of a residual soil. Can. Geotech. J. **32**, 60–77 (1995)
48. Reades, D., Green, G.: Independent stress control and triaxial extension tests on sand. Géotechnique **26**(4), 551–576 (1976)
49. Rechenmacher, A., Finno, R.: Digital image correlation to evaluate shear banding in dilative sands. Geotech. Test. J. **27**(1), 1–10 (2004)
50. Roscoe, K.: The influence of strains in soil mechanics, 10th Rankine lecture. Géotechnique **20**(2), 129–170 (1970)
51. Schanz, T., Vermeer, P.: Angles of friction and dilatancy of sand. Géotechnique **46**(1), 145–151 (1996)
52. Shahnazari, H., Salehzade, H., Askarinejad, A.: Determination of virtual cohesion in unsaturated sand trenches, using geotechnical centrifuge. Int. J. Civil Eng. **6**(1), 1–9 (2009)
53. Stratford, W., Stern, T.: Crust and upper mantle structure of a continental backarc: central North Island, New Zealand. Geophys. J. Int. **166**, 469–484 (2006)
54. Tatsuoka, F., Siddiquee, M., Park, C.S., Sakamoto, M., Abe, F.: Modelling stress-strain relations of sand. Soils Found. **33**(2), 60–81 (1993)
55. Vanapalli, S., Fredlund, D., Pufahl, D., Clifton, A.: Model for the prediction of shear strength with respect to soil suction. Can. Geotech. J. **33**, 379–392 (1996)
56. Vardoulakis, I.: Shear band inclination and shear modulus of sand in biaxial tests. Int. J. Num. Anal. Meth. Geom. **4**, 103–119 (1980).
57. Vendeville, B., Cobbold, P., Davy, P., Brun, J., Choukroune, P. : Physical models of extensional tectonics at various scales. In: 'Coward, M.P., Dewey, J.F., Hancock, P.L. (eds.) Continental Extensional Tectonics, pp. 95–107. Geological Society Special Publication Blackwell Scientific, No. 28, Oxford (1987)
58. Vendeville, B., Cobbold, P.R.: How normal faulting and sedimentation interact to produce listric fault profiles and stratigraphic wedges. J. Struct. Geol. **10**(7), 649–659 (1988)
59. Wanatowski, D., Chu, J.: Strain softening of K_0-consolidated Changi sand under plane-strain conditions. Acta Geotech. **1**, 29–42 (2006)
60. Wanatowski, D., Chu, J.: Drained behaviour of Changi sand in triaxial and plane strain compression. Geomech. Geoeng. **2**, 29–39 (2007)
61. Wanatowski, D., Chu, J., Lo, R.C.: Strain-softening behaviour of sand in strain path testing under plane-strain conditions. Acta Geotech. **3**, 99–114 (2008)
62. Watanabe, K., Koseki, J., Tateyama, M.: Application of high-speed digital ccd cameras to observe static and dynamic deformation characteristics of sand. Geotech. Test. J. **28**(5), 423–435 (2005)
63. Wernicke, B.: Uniform-sense normal simple shear of the continental lithosphere. Can. J. Earth Sci. **22**, 108–125 (1984)
64. Westaway, R.: Continental extension on sets of parallel faults: observational evidence and theoretical models. In: Roberts, A., Yielding, G., Freeman, B. (eds.) The Geometry of Normal Faults, pp. 143–169. Geological Society Special Publication No. 56, The Geological Society, London (1991)
65. White, D., Take, W., Bolton, M.: Soil deformation measurement using particle image velocimetry (piv) and photogrammetry. Géotechnique **53**(7), 619–631 (2003)
66. Wolf, H.: Zur Scherfugenbänderung granularer Materialien unter Extensionsbeanspruchung. Ph.D. thesis, Ruhr-Universität Bochum, Triantafyllidis, Th. (Ed.) (2005). Heft 37
67. Wolf, H., König, D., Triantafyllidis, T.: Experimental investigation of shear band patterns in granular materials. J. Struct. Geol. **25**, 1229–1240 (2003)
68. Wolf, H., König, D., Triantafyllidis, T.: Centrifuge model tests on sand specimen under extensional load. Int. J. Numer. Anal. Methods Geomech. **29**(1), 25–47 (2005)
69. Wolf, H., König, D., Triantafyllidis, T.: The influence of the stress-strain behavior of non-cohesive soils on the geometry of shear band systems under extensional strain. Eng. Struct. **28**, 1760–1773 (2006)
70. Wu, W., Kolymbas, D.: On some issues in triaxial extension tests. Geotech. Test. J. **14**(3), 276–287 (1991)
71. Xiao, H.B., Dahlen, F., Suppe, J.: Mechanics of extensional wedges. J. Geophys. Res. **96**(B6), 10,301–10,318 (1991)
72. Yamamuro, J., Liu, Y.: Effects of necking and its suppression in axisymmetric extension tests on clay. In: Proceedings of the 16th International Conference on Soil Mechanics and Geotechnical Engineering, vol. 2, pp. 633–636. Millpress, Rotterdam (2005)
73. Yamamuro, J.A., Lade, P.V.: Strain localization in extension tests on granular materials. J. Eng. Mech. **121**(7), 828–836 (1995)
74. Yoshida, T., Tatsuoka, F., Siddiquee, M.S.A., Kamegai, Y., Park, C.S. : Shear banding in sands observed in plane strain compression. In: Chambon, R., Desrues, J., Vardoulakis, I. (eds.) Localisation and Bifurcation Theory for Soils and Rocks, pp. 165–179. Balkema, Rotterdam (1994)
75. Zornberg, J., Friedrichsen, J., Dell'Avanzi, E.: Performance of centrifuge data acquisition systems using wireless transmission. Geotech. Test. J. **28**(2), 144–150 (2005)